Geophysical Journal International

Geophys. J. Int. (2017) **210,** 1858–1871
Advance Access publication 2017 June 21
GJI Seismology

doi: 10.1093/gji/ggx271

An algorithm for computing synthetic body waves due to underside conversion on an undulating interface and application to the 410 km discontinuity

Han Zhang,[1,2] Sidao Ni,[1] Risheng Chu[1] and Brandon Schmandt[2]

[1]*State Key Laboratory of Geodesy and Earth's Dynamics, Institute of Geodesy and Geophysics, Wuhan* 400077*, China. E-mail:* sdni@whigg.ac.cn
[2]*Department of Earth and Planetary Science, University of New Mexico, Albuquerque, NM* 87131*, USA*

Accepted 2017 June 20. Received 2017 June 14; in original form 2016 October 20

SUMMARY

The topography of the 410 km discontinuity provides helpful constraints on both petrologic and geodynamic models of the mantle transition zone. Previous studies involving differential times between scattered phases ($S_{410}S$, $p_{410}P$, $s_{410}P$, etc.) and reference phases (SS, P, pP, sP, etc.) have revealed large-scale topography on the 410 km discontinuity. In contrast, amplitude variations of converted phases are more sensitive to smaller scale topography. We develop an algorithm to calculate synthetic *S*-to-*P* conversions at the 410 km discontinuity above deep earthquakes using ray theory and the representation theorem. After benchmarking our method with geometrical ray theory, we perform tests on elevated and depressed topography with dome or ridge shapes. We find that focusing/defocusing due to discontinuity topography substantially alters the amplitudes of converted phases (60 per cent–300 per cent based on our examples). We then use the new algorithm to model amplitude variations of the $s_{410}P$ waves from a deep earthquake beneath western Brazil. A grid search over potential values for the width and height of a ridge-like elevation of the 410 km discontinuity found that the observed amplitude pattern can be explained by a ridge with a height of 12 km and width of 180 km near the expected location of a subducted slab. The new method demonstrated here can be easily adapted to model downgoing $S_{410}P$ or $S_{660}P$ waves, but the representation theorem needs to be combined with numerical solvers to tackle complex 3-D structures near mantle discontinuities.

Key words: Composition and structure of the mantle; Phase transitions; Body waves; Computational seismology; Wave propagation.

1 INTRODUCTION

The globally observed 410 and 660 km discontinuities define the mantle transition zone and are essential in understanding mantle convection processes (Helffrich 2000; Kind & Li 2007). Although phase transitions in olivine polymorphs are believed to be the dominant mechanism for generating the 410 and 660 km discontinuities (Irifune *et al.* 1998), the pyroxene and garnet components are needed to account for the complicated nature of the seismologically observed 660 km interface (Weidner & Wang 1998; Deuss *et al.* 2006). Assuming that these two mantle interfaces are respectively associated with positive and negative Clapeyron slopes arising from phase changes in olivine polymorphs (Ringwood 1969; Bina & Wood 1986; Deuss *et al.* 2006), the 410 km discontinuity should be elevated and the 660 km discontinuity should be depressed at lower temperatures near subducted slabs, and vice versa, at higher temperatures near upwelling regions (Davis *et al*. 1989; Wicks & Richards 1993; Helffrich & Bina 1994; Tibi & Wiens 2005). But the phase transition near 660 km depth for a pyrolite mantle may also display a positive Clapeyron slope if the local mantle temperature is above 1800 °C (Weidner & Wang 2000). In order to estimate thermal structures and to understand petrologic and geodynamic processes in the mantle transition zone, numerous seismological studies have been performed to map topography of the 410 and 660 km discontinuities.

Although free oscillation data have been adopted in mapping mantle discontinuities (Ishii & Tromp 1999), seismic body waves are more commonly used to determine relief of these mantle interfaces. This is mainly because of body wave penetrating power. Body wave methods for investigating the 410 and the 660 topography can be categorized into one of the following two groups: turning waves or triplications which sample mantle interfaces almost horizontally (Song *et al.* 2004; Wang & Niu 2010; Chu *et al.* 2012; Wang *et al.* 2014), or scattering of steeply incident waves which may occur near the midpoint, receiver side, or source side. In studies with the midpoint reflection approach, researchers usually utilize the differential time between *SS* or *PP* and their precursors on long-period seismograms (Flanagan & Shearer 1998a, 1999; Chambers *et al*. 2005;

Deuss *et al*. 2006; Schmerr & Garnero 2007; Houser *et al*. 2008; Cao *et al*. 2011), although short-period data have been used for $P'P'$ precursors (Benz & Vidale 1993; Xu *et al.* 2003; Day & Deuss 2013). Less limited by the geographical distribution of earthquakes and stations, these methods provide almost global coverage of the 410 and the 660 sampling. Using *SS* and *PP* precursors, Flanagan & Shearer (1998a, 1999) mapped the global topography of the 410 km discontinuity and reported a peak-to-peak variation of about 30 km across horizontal scales of thousands of kilometres. To reveal topography on smaller scales, receiver side methods are used and among them teleseismic *Ps* receiver function analysis is a popular approach. When dense array data are available, researchers are able to obtain high-resolution images of upper-mantle discontinuities through stacking of receiver functions (e.g. Li *et al.* 2000; Helffrich *et al.* 2003). Recently, Thompson *et al.* (2011) used teleseismic receiver functions to image upper-mantle discontinuities and concluded that the transition zone structures beneath the cratonic core of North America are uniform and simple.

The source side approach provides another way of mapping small-scale topography. It takes advantage of simple source time functions and the weak coda of the direct *P* waves from deep earthquakes, which makes it easier to identify later *P* arrivals converted from transmitted *S* waves or reflected *P* (or *S*) waves. This approach can yield high spatial resolution due to small Fresnel zones and thus provides a powerful tool for detecting small-scale topography of mantle interfaces. Collier & Helffrich (1997) tested the effects of a subducted slab on the 410 and the 660 in the Izu–Bonin area by studying the $p_{410}P$ and $s_{410}P$ waves due to underside *P*- or *S*-to-*P*-wave conversions at the 410 km discontinuity. After measuring the differential traveltime and slowness between the converted phases and the direct *P* waves, they mapped the topography of these two discontinuities. Their results corroborated the anticorrelation of the depth of the 410 and the 660 near the Izu–Bonin subducted slab, which is consistent with the prediction from the phase changes origin hypothesis. Flanagan & Shearer (1998b) used relatively long period near source data, for example, $s_{410}P$ and $s_{410}S$, to study the 410 km discontinuity near a subduction zone. Their result suggested that large depth variations, if they exist, are limited to a narrow zone within the slab.

In previous near source studies, discontinuity topography was constrained with only differential traveltime data, which can be accurately measured with cross-correlation methods for dense array recordings. However, a locally flat interface is usually assumed when mapping the topographic variations, which is seemingly paradoxical. Instead, amplitude information from the converted waves should be able to provide further constraints on topography of mantle velocity discontinuities (Chaljub & Tarantola 1997; Deng & Zhou 2015). For example, van der Lee *et al.* (1994) computed synthetic *P* and $P_{660}s$ waves by applying the Kirchoff integral over an undulating 660 km interface, and found amplified or reduced $P_{660}s$ waves due to focusing or defocusing effects. Similar approaches have been adopted in modelling other interfaces such as the core–mantle boundary (CMB). Kampfmann & Muller (1989) calculated synthetic short-period (1 s) *PcP* waves for some CMB models, which feature sinusoidal topography with wavelength, *L*, and amplitude, *E*. By varying *L* and *E*, they found that for a large-scale topography model, that is, $L \geq 100$ km, *PcP* energy is focused by topographic valleys and defocused by domes. In contrast, for the cases of smaller scale ($L \leq 50$ km), *PcP* amplitude is lower than that of the reference case. These synthetic modelling results are in agreement with the seismological observations of the *PcP* wave at distances beyond 70°. The results of Neuberg & Lisapaly (1997) also indicated that different topographic wavelengths and elevations of the CMB had complicated effects on amplitudes of the *PcP* waves. More recently, Wu *et al.* (2014) computed synthetic *PcP* seismograms using the representation theorem and they confirmed that a depressed CMB topography with 6 km depth variations over a horizontal scale of 300 km is capable of amplifying short-period *PcP* waves by a factor of 4–6. Additionally, the topography of the discontinuities may distort the reflected waveforms, which could also be used in inferring the topography (van der Lee *et al.* 1994).

In this paper, we develop an algorithm for computing synthetic *S*-to-*P* conversions at an interface above deep focus earthquakes based on the combination of ray theory and the representation theorem. After benchmarking this method with the geometric ray theory, we test the effects of different topographies on amplitudes of the converted *P* waves. We then use this method to study the topography of the 410 km discontinuity revealed by the $s_{410}P$ waves of a deep earthquake beneath western Brazil and discuss the advantages and limitations of the algorithm.

2 METHODS

There are various methods for computing synthetic body waves for both 1-D layered Earth models (spherical symmetry) and 3-D heterogeneous Earth models. The propagator matrix method provides a fast tool for generating full-waveform synthetics with a 1-D Earth model (Haskell 1964; Zhu & Rivera 2002), and is useful when the regions of interest can be characterized by horizontally layered media. However, various studies have demonstrated that there are obvious 3-D structures inside the Earth and their interactions with seismic waves may distort the waveforms substantially (Lay *et al.* 1998; Ritsema *et al.* 1999; Ni *et al*. 2002; Rost & Revenaugh 2004; Bai & Ritsema 2013; Schmerr *et al*. 2013; Lessing *et al*. 2015). In these cases, methods for computing synthetic seismograms for a 3-D model are needed either for forward modelling or inversion studies. Approaches such as finite-difference (FD) and spectral element methods (SEM) solve the seismic wave equation numerically and provide accurate results, but require costly computational facilities (Igel & Weber 1995; Komatitsch & Tromp 1999). For example, Tsuboi *et al.* (2004) used 4056 processors of the Earth simulator, one of the largest machines in the world at that time, to model seismic wave propagation globally and their result was accurate only to a period of 3.5 s. As the $s_{410}P$, $p_{410}P$ or other later *P* arrivals caused by the mantle interfaces are usually observed with high signal-to-noise ratio at shorter periods (around 1 Hz), those numerical methods would be very time consuming for simulating converted *P* waves globally. In contrast, seismic ray theory may be applied to compute short-period synthetic seismograms for mildly heterogeneous velocity structures with much improved efficiency. Researchers have adopted methods including the Kirchhoff integral, the representation theorem, WKBJ, Maslov asymptotic theory or WKM in modelling discontinuity topography or volumetric heterogeneities (Chapman 1978; Chapman & Drummond 1982; Kampfmann & Muller 1989; van der Lee *et al.* 1994; Ni *et al.* 1999; Shen *et al.* 2016). Following Wu *et al.*(2014), we adopt the representation theorem (Aki & Richards 2002) in combination with ray theory to deal with 3-D topography. Theoretically, this approach is equivalent to the Kirchoff integral method, but the former can be readily extended to the case of strong volumetric heterogeneity, where the stress and displacement field can be accurately retrieved with 3-D wave equation solvers. With the representation theorem (Aki & Richards 2002), displacement at remote receivers is obtained from integration of traction T_i and displacement U_i on the interface Σ, which is,

$$u_n(\vec{x},t)=\int_{-\infty}^{+\infty}d\tau\iint\left\{G_{in}\left(\vec{\xi},t-\tau;\vec{x},0\right)T_i\left(\vec{U}(\vec{\xi},\tau),\vec{n}\right)\right.$$
$$\left.-U_i\left(\vec{\xi},\tau\right)c_{ijkl}n_jG_{kn,l}\left(\vec{\xi},t-\tau;\vec{x},0\right)\right\}d\Sigma\left(\vec{\xi}\right)\quad(1)$$

where τ and $G(\vec{\xi},\vec{x})$ are the delay time and Green's function between an area of elements on $\Sigma(\vec{\xi})$ and receivers $\vec{x}$ respectively, $\vec{n}$ is normal vector on $\Sigma(\vec{\xi})$ and c_{ijkl} is elastic stiffness tensor. The displacement U on the interface and the Green's function $G(\vec{\xi},\vec{x})$ between an area of elements on Σ and receivers $\vec{x}$ can be calculated from the following two equations with ray theory (Cerveny 2005):

$$U\left(\vec{S},\vec{\xi}\right)=\frac{\left(\vec{F}\cdot\overleftrightarrow{M}\cdot\vec{A}\right)Ref}{4\pi\rho^{\frac{1}{2}}\left(\vec{S}\right)\rho^{\frac{1}{2}}\left(\vec{\xi}\right)\beta^{\frac{5}{2}}\left(\vec{S}\right)\beta^{\frac{1}{2}}\left(\vec{\xi}\right)R^{SV}_{S-\xi}\left(\vec{S},\vec{\xi}\right)}\quad(2)$$

$$G\left(\vec{\xi},\vec{x}\right)=\frac{1}{4\pi\rho^{\frac{1}{2}}(\vec{x})\rho^{\frac{1}{2}}\left(\vec{\xi}\right)\alpha^{\frac{3}{2}}(\vec{x})\alpha^{\frac{1}{2}}\left(\vec{\xi}\right)R^{P}_{x-\xi}\left(\vec{x},\vec{\xi}\right)}\quad(3)$$

Then, the displacement of the S-to-P conversion at remote receiver $\vec{x}$ is calculated from the following equation:

$$\vec{u}(\vec{x},t)=-\int_{-\infty}^{+\infty}d\tau\iint U\left(\vec{S},\vec{\xi}\right)G\left(\vec{\xi},\vec{x}\right)\vec{D}\left(\vec{\xi}\right)\alpha^{-1}\left(\vec{\xi}\right)$$
$$\times\{[\lambda(\vec{E}\cdot\vec{N})+2\mu(\vec{E}\cdot\vec{C})(\vec{N}\cdot\vec{C})]$$
$$\times\dot{f}\left(\tau-T^{SV}_{S-\xi}\right)\delta\left(t-\tau-T^{P}_{x-\xi}\right)$$
$$-\left[\lambda\left(\vec{C}\cdot\vec{N}\right)+2\mu\left(\vec{C}\cdot\vec{E}\right)\left(\vec{N}\cdot\vec{E}\right)\right]f\left(\tau-T^{SV}_{S-\xi}\right)$$
$$\times\ \dot{\delta}\left(t-\tau-T^{P}_{x-\xi}\right)\}d\Sigma\left(\vec{\xi}\right)\quad(4)$$

where λ and μ are Lame constants, ρ is density and α and β are the P- and S-wave velocity, respectively. The traveltime from the earthquake source to the converted point is denoted as $T^{SV}_{S-\xi}$ and the traveltime from the receiver to the conversion point is $T^{P}_{x-\xi}$. $\overleftrightarrow{\boldsymbol{M}}$ represents the moment tensor of the earthquake following the Aki & Richards (2002) convention and $f(t)$ is the source time function, while $\delta(t)$ is the Dirac delta function. *Ref* is the conversion coefficient of P–P or SV–P reflection at the interface Σ, which can be the free surface or a mantle discontinuity, and the reflection coefficient is taken from eqs (5.27) and (5.31) and (5.40), respectively, in Aki & Richards (2002). $R^{SV}_{S-\xi}$, and $R^{P}_{x-\xi}$ represent the effect of geometry spreading. $\vec{N}$ is the unit normal vector to Σ, and unit vectors $\vec{A},\vec{B},\vec{C},\vec{D},\vec{E},\vec{F}$ and $\vec{G}$ are defined in Fig. 1. Since we are more concerned with topographic variations of mantle discontinuities, we assume the PREM 1-D Earth model (Dziewonski & Anderson 1981) for ray tracing to compute the traveltime T and the geometric spreading factor R. The integration over the interface Σ is achieved via summation of contributions from all gridpoints, which are meshed in longitude (with interval of dx) and latitude (with interval of dy) directions.

First, we benchmark our algorithm by comparing the synthetic teleseismic sP wave computed with the representation theorem for the case of a flat-free surface and synthetics calculated with geometrical ray theory for a 1-D Earth model (Kikuchi & Kanamori 1982). The earthquake we used here is placed at a location of longitude = 0° and latitude = 0°. A focal depth of 100 km is adopted so that the sP signal is sufficiently isolated from the pP and P waves.

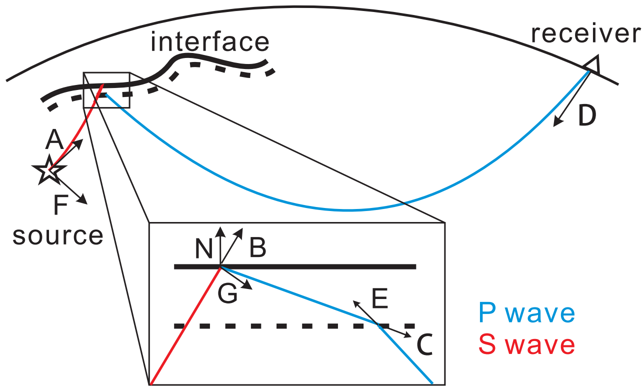

Figure 1. Schematic configuration of wave vectors and ray paths used in the synthetic method. Blue and red lines denote ray path of P and SV waves, respectively. Theoretically, the integration in eq. (1) is performed on a virtual interface (bold dashed curve) immediately below the true interface (bold solid curve). **N** is the normal vector on the interface. **A** and **F** are takeoff vector and polarization of the SV wave leaving the source (star), while **B** and **G** are those of incident SV wave on the interface. **D** and **E** are polarization vectors of the P wave at receiver and on the virtual interface. **C** is the polarization vector of the P wave converted from SV wave following Snell's law.

The moment tensor is chosen to be Mrr = −4.0e18, Mtt = 3.0e18, Mff = 1.0e18, Mrt = 2.0e18, Mrf = −1.0e18 and Mtf = −1.0e18 with unit N·m. A Ricker wavelet with centre frequency of 1.0 Hz is used as the source time function because the P wave near this frequency is often observed with a high signal-to-noise ratio (Earle & Shearer 1997). The sampling rate is 0.05 s, which is commonly available from GSN (Global Seismic Network) stations. The intervals of longitude (dx) and latitude (dy) at free surface are set to 0.005°, which is small enough to guarantee that the traveltime difference between neighbouring elements is less than the sampling rate. Smaller dx and dy do not improve synthetic seismograms appreciably. Synthetic seismograms are then computed for a linear array of receivers with a constant azimuth of 90°. For an interface of 1.6×10^5 elements with 30 receivers, it takes about 600 s to calculate the synthetics on one CPU (2.5 GHz). Considering that synthetics for different stations are highly independent, 20 CPU·s is a reasonable estimate for a single seismogram. Coherent direct P, pP and sP waves are clearly observable on the synthetic seismograms from geometric ray theory (Fig. 2). The sP wave lags behind the direct P wave by about 34 s, which can be explained with a focal depth of 100 km.The differential time increases at longer distances, consistent with smaller takeoff angles of the sP wave at more distant receivers. The synthetic sP waveforms from the representation theorem provide a good match to both the amplitudes and arrival times of the sP waveforms from geometric ray theory, with a normalized L2 waveform misfit less than 0.08.

Next we proceed to investigate the effects of an undulating free surface on amplitudes and traveltimes of the sP wave. Although our method is applicable to more complicated topography, we only test two simplified types of topography, a hemispherical dome analogous to the effect of a hot narrow plume and a ridge-like feature analogous to the effect of a cold subducted slab. The dome topography is defined as:

$$h(x,y)=\begin{cases}\frac{1}{2}H\left(1+\cos\left(2\pi*\frac{r}{L}\right)\right), & r<L/2\\ 0, & r\geq L/2\end{cases}\quad(5)$$

where h is the topography variation at point (x, y). L and H are diameter and height of the dome respectively. r is the distance

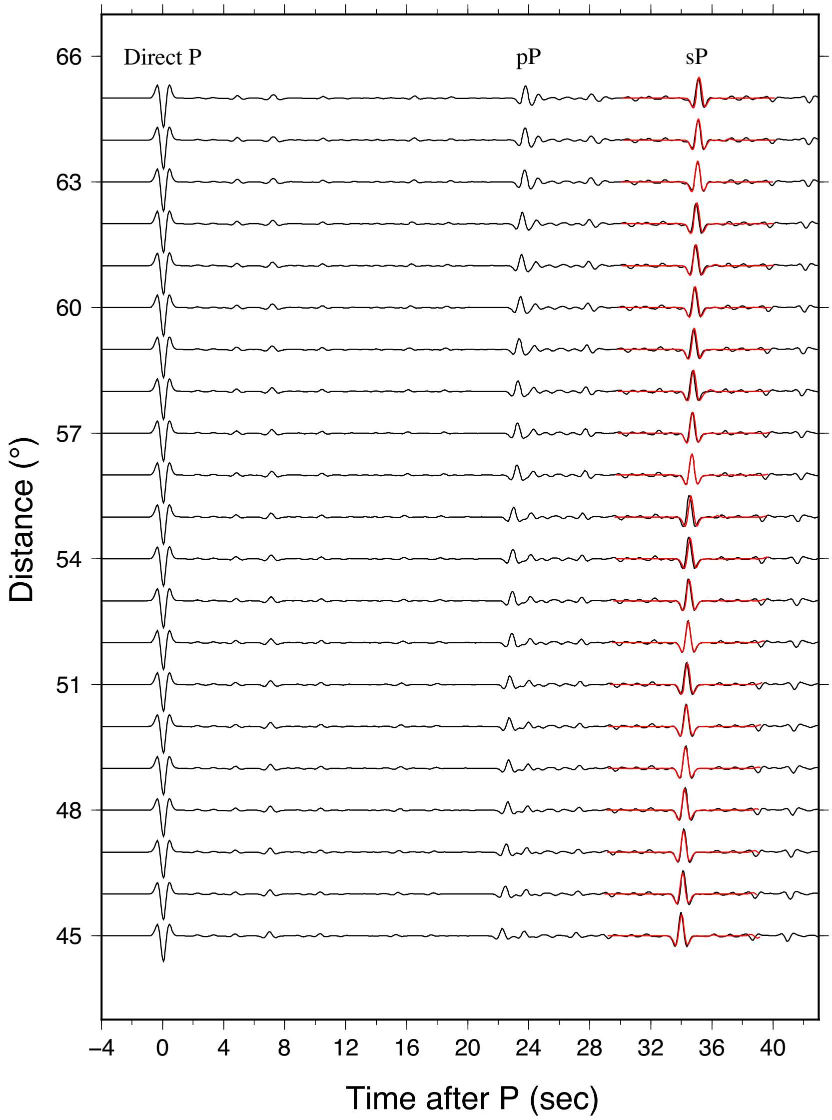

Figure 2. Synthetic waveforms of *P*, *pP* and *sP* computed with geometrical ray theory (black) (Kikuchi & Kanamori 1982) and our method (red). Only the *sP* wave is compared. Other phases such as the *P* and *pP* waves are not calculated in our algorithm.

between the point (*x, y*) and the centre of the dome. Similarly, the ridge-like topography is defined as:

$$h(x, y) = \begin{cases} \frac{1}{2}H\left(1 + \cos\left(2\pi * \frac{d}{L}\right)\right), & d < L/2 \\ 0, & d \geq L/2 \end{cases} \tag{6}$$

where *d* is the distance between the point (*x, y*) and the ridge peak line. For demonstration purposes, *H* is chosen to be + 2 km (elevated) or −2 km (depressed), and *L* is chosen to be 100 km.The centre of the dome is placed at longitude = 0° and latitude = 0.29°, to coincide with the bounce point of the *sP* wave at the free surface for an epicentral distance of 45°. The crest of the ridge-like topography strikes along an azimuth of 90° through the point of longitude = 0° and latitude = 0°. In order to explore the effects of frequency, source time functions with centre frequencies of 1.0 and 0.15 Hz are tested.

In Fig. 3(a), the synthetic *sP* waves are displayed for the cases of an elevated dome (red traces) and a flat surface (black traces). At 1.0 Hz, the *sP* signals are delayed by about 0.90 s near a distance of 45°, close to the delay due to 2 km elevation which is around 0.97 s for $Vs = 3.2$ km s^{-1} and $Vp = 5.8$ km s^{-1} in the upper crust of the PREM model. The elevated dome results in large-amplitude variations, with the *sP* signals amplified by a factor of 2.3–3.2. The maximum amplification occurs between 45° and 48°, which could be caused by focusing effects of the dome. For the 0.15 Hz case, the *sP* signals are less delayed and less amplified, probably due to a larger Fresnel zone and reduced focusing effect. In contrast, for the case of a depressed dome (Fig. 3b), the *sP* signals are advanced in traveltime and reduced in amplitude, consistent with a smaller propagation distance of the *sP* wave and defocusing effects. Although the absolute amplitudes of the *sP* wave could be affected by factors such as radiation pattern and earthquake magnitude, the unusual variation with epicentral distance could be a signature of an undulating discontinuity topography. Moreover, it seems that the focusing effect is stronger than the defocusing effect. For example, the 1.0 Hz *sP* wave is magnified by a factor of about 3 for the elevated case and its amplitude is reduced to about 0.6 for the depressed topography case at a distance of 45°, which is likely caused by non-linear interference effects. For the case of ridge-like topography (Figs 3c and d), the effects are similar

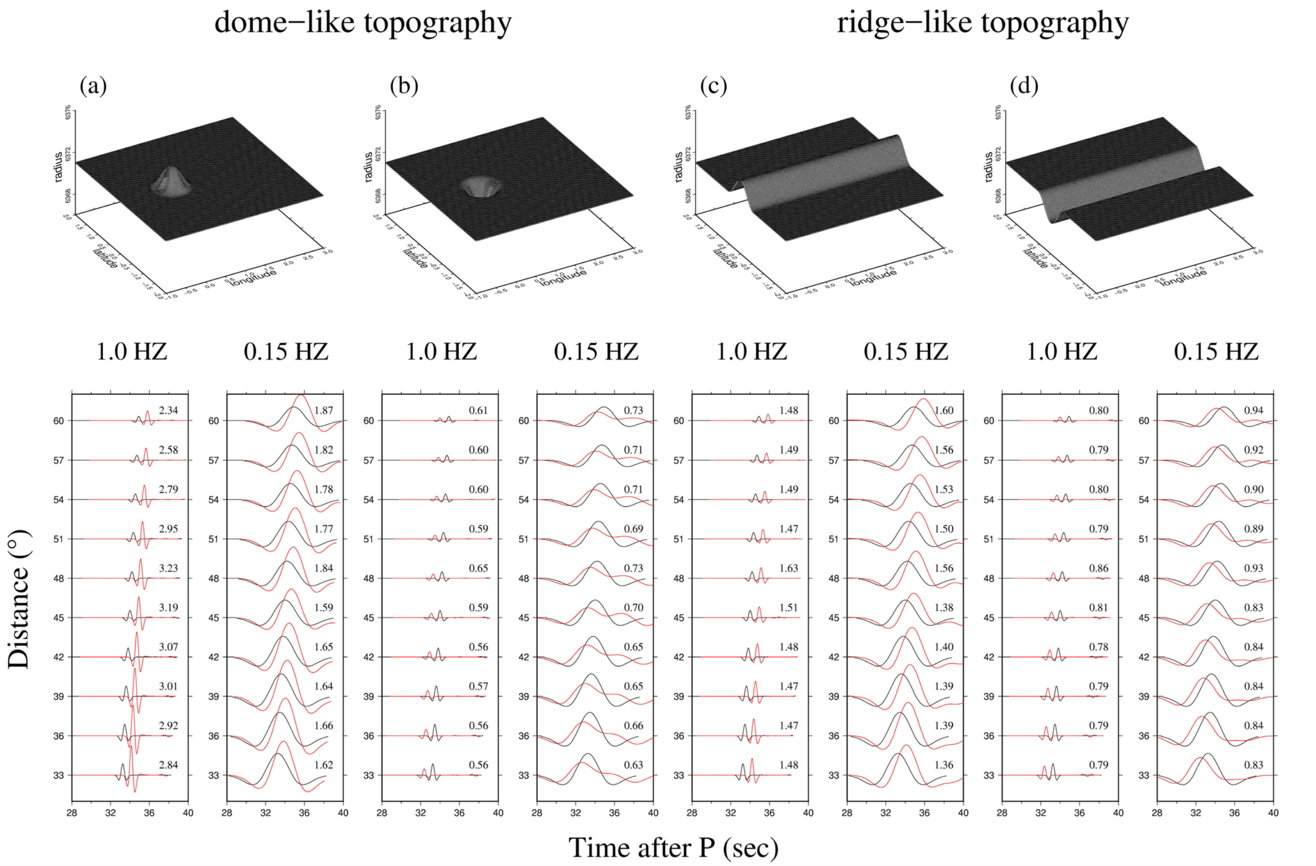

Figure 3. Synthetic *sP* phase (red) computed with our method for different topographies and different frequencies. Black lines are results for a flat 1-D Earth model. Peak-to-peak amplitude ratios between the *sP* signal of topography and those of a flat interface are indicated on the right-hand side.

to those for the case of dome-like topography, but less pronounced. This is not surprising because the ridge structures focus or defocus seismic waves along only one direction (perpendicular to ridge line direction).

After demonstrating that the algorithm works for the case of the *sP* wave from free-surface reflection, we proceed to apply the algorithm to study topography of the 410 with the reflected phase $s_{410}P$ from a deep earthquake in South America.

3 APPLICATION

3.1 Data processing

Array data for deep earthquakes are usually needed for studies of weak $p_{410}P$ and $s_{410}P$ signals. These signals can be enhanced with beamforming techniques (Rost & Thomas 2002). The USArray is a preferred data set in studying near source conversions for its large aperture and relatively dense station spacing. The USArray has been extensively used to study mantle interfaces and small-scale scattering (e.g. Li *et al.* 2008; Niu 2014; Schmandt *et al.* 2014). To augment spatial coverage, we also adopt stations in the CI, UW and US networks (Fig. 4). Given this set of seismographs, the sampling points of converted waves should be close enough to the intersection of a subducted slab and the 410 to make any potential amplification effects due to discontinuity topography detectable. The South American subduction zone features earthquakes with depths up to 700 km, some of which are located within the preferred distance range (30°–90°). After examining five of them, we selected a M_w 6.5 earthquake that occurred below western Brazil on 2010 May 24 (Table 1). Events with magnitudes less than 6.0 would produce $p_{410}P$ and $s_{410}P$ waves too weak for analysis, while the source time functions of earthquakes larger than M_w 7.0 are more complicated and lead to challenges in waveform modelling.

Broad-band vertical component seismograms for the time window 1 min before and 20 min after the *P*-wave arrival of the deep earthquake were requested from the IRIS DMC. The raw waveform data were first pre-processed by removing the mean and detrending, and converting the signals to ground displacement using the instrument response function. Next the seismograms were band-pass filtered between 1 and 5 s period. Only traces with the *P*-wave signal-to-noise ratio greater than 5 were kept for further studies (Niu 2014). In Fig. 5(a), a record section showing the *P* wave and later arrivals is displayed with all the traces aligned along the arrival time of the direct *P* wave. The depth phases *pP* and *sP* are clear and coherent, and they can be used to improve focal depth estimation, which is needed for modelling the $s_{410}P$ wave. By modelling the differential time between the depth phases and the direct *P* wave, we determined the focal depth to be 580 km via a grid search with a 1 km depth interval. Although the depth is 10 km shallower than Global CMT solution, it is close to the ISC (International Seismological Centre) depth estimate of 582.1 km. Moreover, the *PcP* and *pPcP* waves are also coherent, again demonstrating the high quality of USArray waveform data. We also observe a clear signal that lags about 40 s behind the direct *P* wave and has similar slowness as the direct *P* wave. This signal could either be associated with reflection/transmission at the 410 or the 660 discontinuity or with scattering from heterogeneity in the lower mantle (Collier &

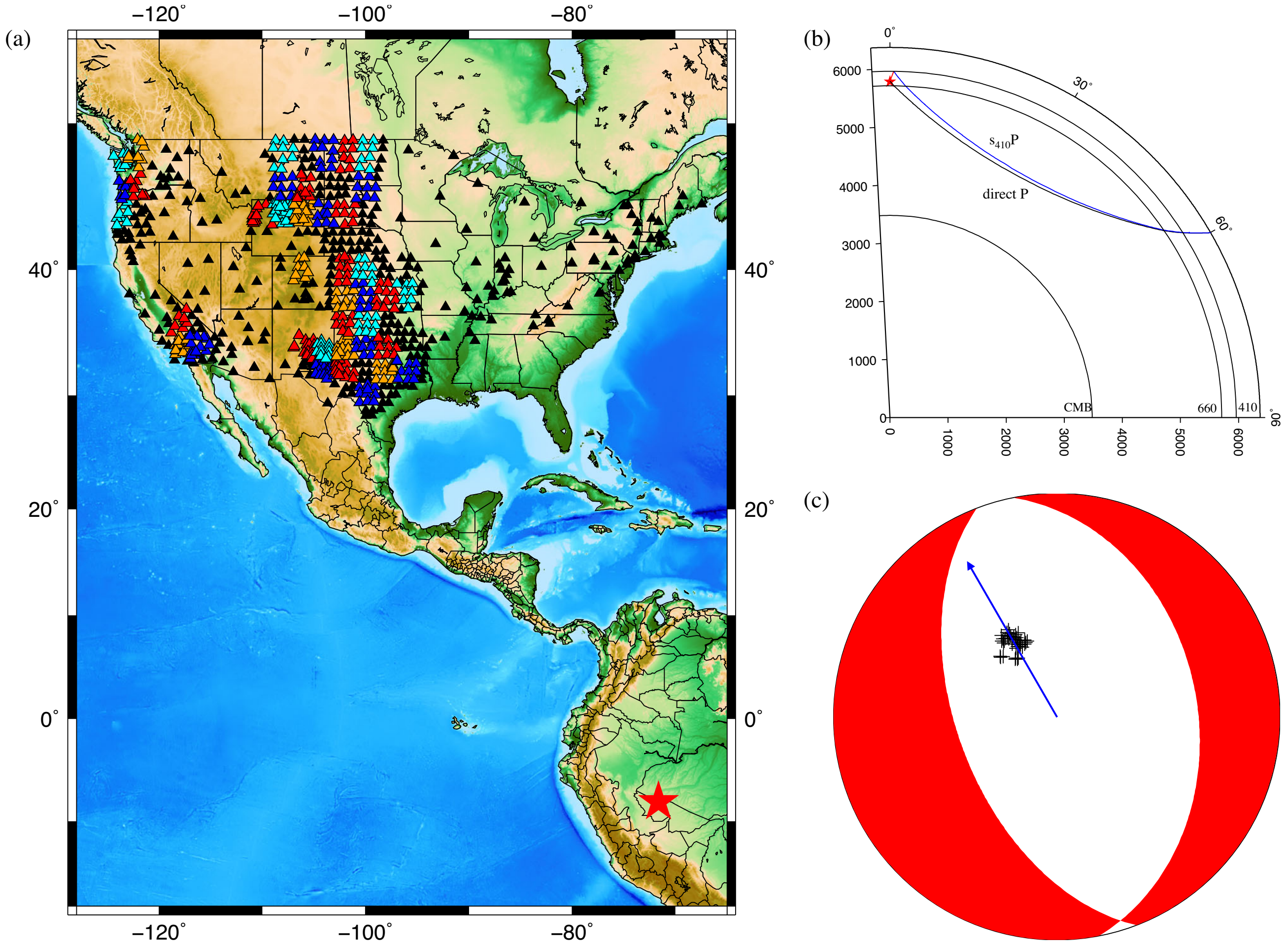

Figure 4. (a) Seismic stations (triangle) and the earthquake (star). Colourful stations are subarrays used for amplitude measurement. (b) Ray path of the direct P and $s_{410}P$ waves at epicentral distance of 60° for the reference 1-D model IASP91. (c) Global CMT moment tensor of the earthquake we use here. Black crosses indicate the projected points of the P wave arriving at the geometric centres of subarrays we selected. Blue line denotes an azimuth of 330°.

Table 1. Earthquake information from GCMT/ISC catalogue.

Origin time		Epicentre		Depth (km)			M_w
Date	Time	Latitude	Longitude	GCMT	ISC*	pP–P	
2010 May 24	16:18:33.6	−8.08°	−71.64°	591.4	582.1	580	6.5

*International Seismological Centre, On-line Bulletin, http://www.isc.ac.uk, Internatl. Seis. Cent., Thatcham, United Kingdom, 2013.

Helffrich 1997; Niu 2014). The S-to-P conversion at the 660 km discontinuity would be too early given the focal depth of 580 km. The 40 s lag time could be explained with an underside S-to-P conversion at the 410 km discontinuity or scattering at about 1000 km depth. But the former would produce a converted P wave with a slowness greater than the direct P wave, while the latter would produce a converted wave with a smaller slowness. Therefore, we determine the slowness of the seismic phases in Fig. 5(a) with frequency–wavenumber analysis (*fk*) and a third-root stacking technique.

We use the software package by Rost & Thomas (2002) to perform *fk* analysis, which can resolve both slowness and backazimuth of coherent arrivals. The *fk* analysis results for the direct P wave and 40 s later arrival are displayed in Fig. 5(b). For the direct P wave, a time window of 5 s before and 10 s after P is adopted. For the later arrival, a 50 s time window is chosen starting 35 s after the first P wave enters the array. On the subpanel for the direct P wave, the energy maximum is situated at a slowness of 7.14 s deg^{-1} and backazimuth of 133.7°. The observed slowness is close to the theoretical value of 7.21 s deg^{-1} and the backazimuth is 3.2° away from the great circle path (backazimuth = 136.9°), implying relatively simple propagation effects along the P-wave path. The slowness and backazimuth of the later arrival are very close to those of the direct P wave, suggesting very similar propagation paths. In order to improve the relative slowness and differential time resolution, we apply third-root stacking with the P-wave backazimuth measured from *fk* analysis. Before stacking, all traces are aligned along the direct P wave and their amplitudes are normalized to the peak amplitude of the direct P wave (Li *et al.* 2008; Niu 2014). On the vespagram (Fig. 5c), the strongest signal is the direct P wave located at time = 0 s and relative slowness = 0 s deg^{-1}, because it is used as the reference phase. The PcP and pP waves are also clearly observed with relative slowness and differential time close to the predictions from IASP91 (Kennett *et al.* 1995), consistent with visual inspection in Fig. 5(a). The signal occurring 40 s later is clear with slowness 0.13 s deg^{-1} greater than the direct P wave, and is close to the prediction of S-to-P conversion at the 410 km discontinuity. However, the timing of the later phase is more consistent with a conversion depth at 425 km, if the focal depth is 580 km. Another weak signal is seen about 20 s after the direct P wave is observed. This signal could be the P-to-P reflection from about 425 km depth (Fig. 5c). Previous studies also reported that the 410 is deeper than normal in this area. For instance, the global

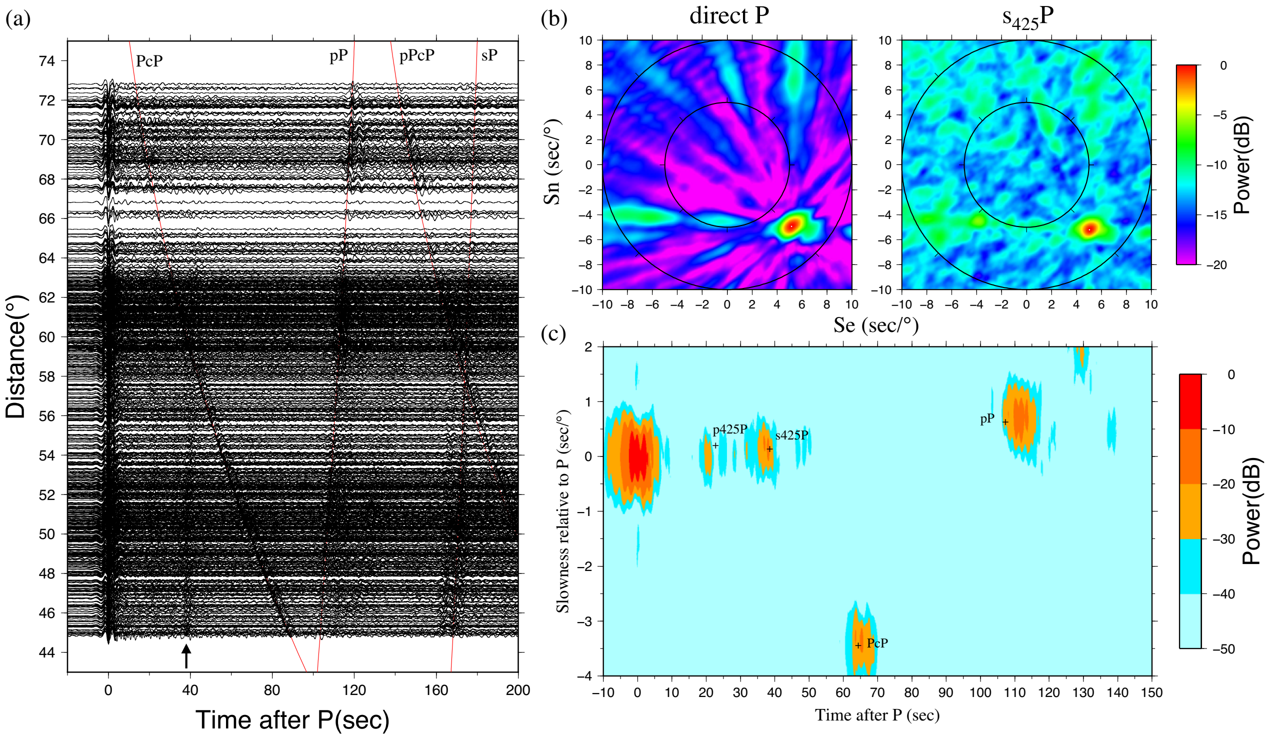

Figure 5. (a) Record section of vertical component waveforms for the earthquake (with GCMT code 201005241618A) aligned with the peak amplitude of the direct P wave. Theoretical differential traveltime of the PcP, pP and sP waves are indicated with red lines. (b) *fk* analysis of the direct P (left-hand panel) and $s_{425}P$ (right-hand panel) waves. (c) third-root stacking of seismograms with data from XR array. Warmer colour represents higher normalized power and may indicate arrivals. Theoretical differential slowness and traveltime are marked with black crosses.

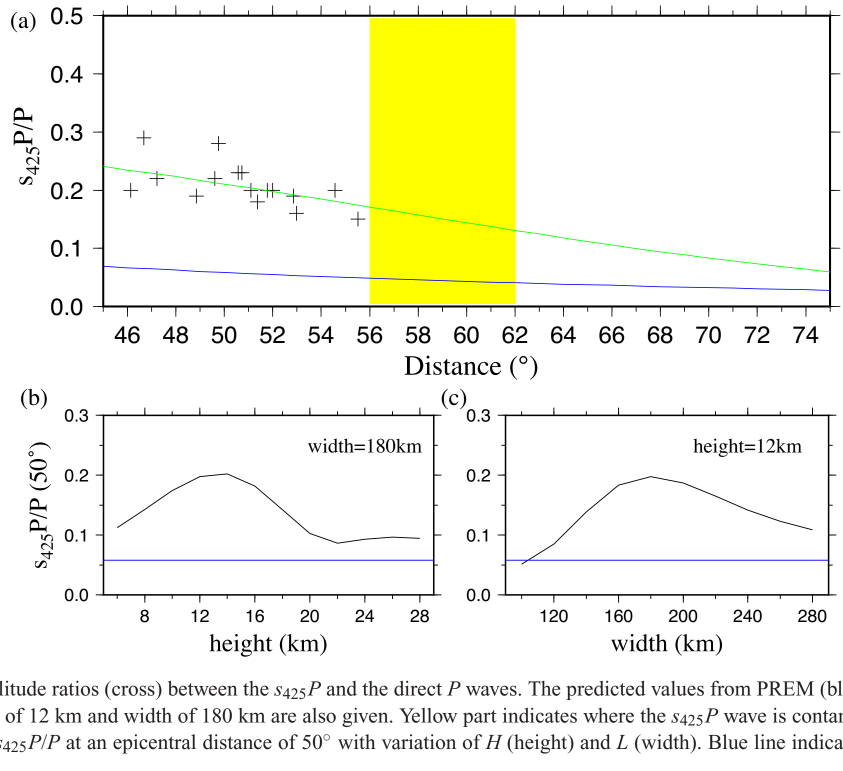

Figure 6. (a) Observed amplitude ratios (cross) between the $s_{425}P$ and the direct P waves. The predicted values from PREM (blue) and an elevated ridge-like structure (green) with height of 12 km and width of 180 km are also given. Yellow part indicates where the $s_{425}P$ wave is contaminated by the PcP phase. (b) and (c) Calculated ratios of $s_{425}P/P$ at an epicentral distance of 50° with variation of H (height) and L (width). Blue line indicates theoretical ratios from the PREM model.

topography of the 410 estimated by Houser *et al.* (2008) indicated the discontinuity is depressed to a position deeper than 418 km depth here. Regional research conducted by Schmerr & Garnero (2007) also suggested the 410 is deeper by up to 10–15 km. In this case, these two signals are less likely to be generated by S-to-P scattering in the lower mantle, which usually leads to smaller slowness than the direct P wave (Niu 2014). Since the $p_{425}P$ signal is much weaker, we only proceed to study the $s_{425}P$ wave.

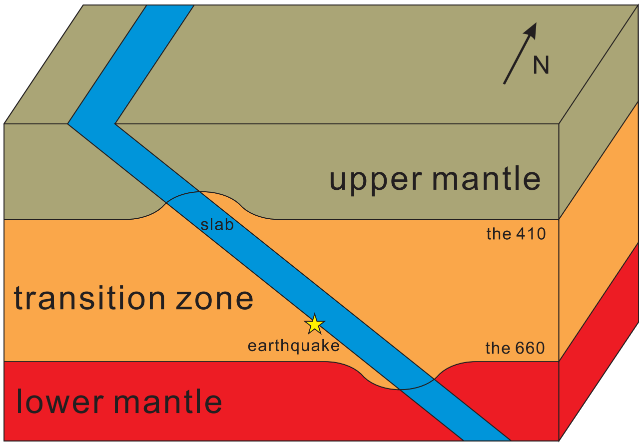

Figure 7. Cartoon for the elevated topography at the 410 km discontinuity. The strike of the slab in this area is approximately north based on the result of Slab 1.0.

Although the relative slowness and differential time have been explained by a deeper than average 410 km discontinuity in this region, the $s_{425}P$ wave is unusually strong compared to expectations for flat mantle interfaces. On many individual traces, the $s_{425}P$ wave can easily be identified with an amplitude ratio relative to the direct P wave of up to 0.3, while predicted values from 1-D reference models are much smaller (0.03–0.07 for PREM and 0.03–0.09 for IASP91). Moreover, it seems that the $s_{425}P$ wave becomes weaker at distances greater than 56°. Considering the fact that the signal-to-noise ratio of the $s_{425}P$ wave in Fig. 5(a) is not high (mostly less than 3), we apply the *fk* analysis and stacking method on subarrays of USArray to obtain reliable amplitude ratio estimates. We first divide the receiver array into 2° (latitude) by 2° (longitude) subarrays and only those with more than eight stations are selected for further studies (Fig. 4a). For each subarray, the P waves are stacked after alignment along the peak amplitude, and the $s_{425}P$ waves are stacked with the slowness and backazimuth measured with *fk* analysis. The backazimuths of the $s_{425}P$ wave observed on all the subarrays are close to the great circle path. Therefore, the amplitude ratios are plotted as a function of epicentral distance (Fig. 6). For the subarrays with epicentral distances beyond 62°, *fk* analysis failed to detect the $s_{425}P$ signal. This is probably due to its low signal-to-noise ratio. Amplitude ratio measurements near epicentral distance of 59° are discarded because of contamination by the *PcP* wave. Predicted $s_{425}P/P$ amplitude ratios with PREM are also displayed in Fig. 6. The observed amplitude ratios are in the range of 0.15–0.29, about four times larger than predicted PREM values. Moreover, from epicentral distances of 46°–56°, the observed ratio decreases by about 50 per cent, while the ratio predicted by PREM decreases much less.

3.2 Alternative explanations

Following Rost & Revenaugh (2004), who observed anomalously large *PcP* to *P* amplitude ratios as well as strong spatial variations, there are a number of mechanisms which may contribute to the large-amplitude ratios we observe here. Potential mechanisms considered below include:

(1) High attenuation of the direct P wave or low attenuation along the $s_{425}P$ wave path.
(2) Error in the CMT moment tensor (Dziewonski *et al.* 1981; Ekström *et al.* 2012).
(3) Unusual velocity contrast across the 410 km discontinuity in this area.
(4) Multipathing and 3-D effects of the slab.
(5) Topography of the 410 km discontinuity near the conversion point.

We first discuss the possible contributions from attenuation. It can be seen from Fig. 4(b) that the ray paths of the direct P and $s_{425}P$ waves are very close except in the near source region. If high attenuation material exists right below the source, it may decrease the amplitude of the direct P wave, and consequently increase the amplitude ratios. However, the clear observation of the downgoing *PcP* wave at almost every station argues against this hypothesis. Additionally, the short distance before the ascending S wave converts to a P wave at the 410 makes a potential low attenuation along

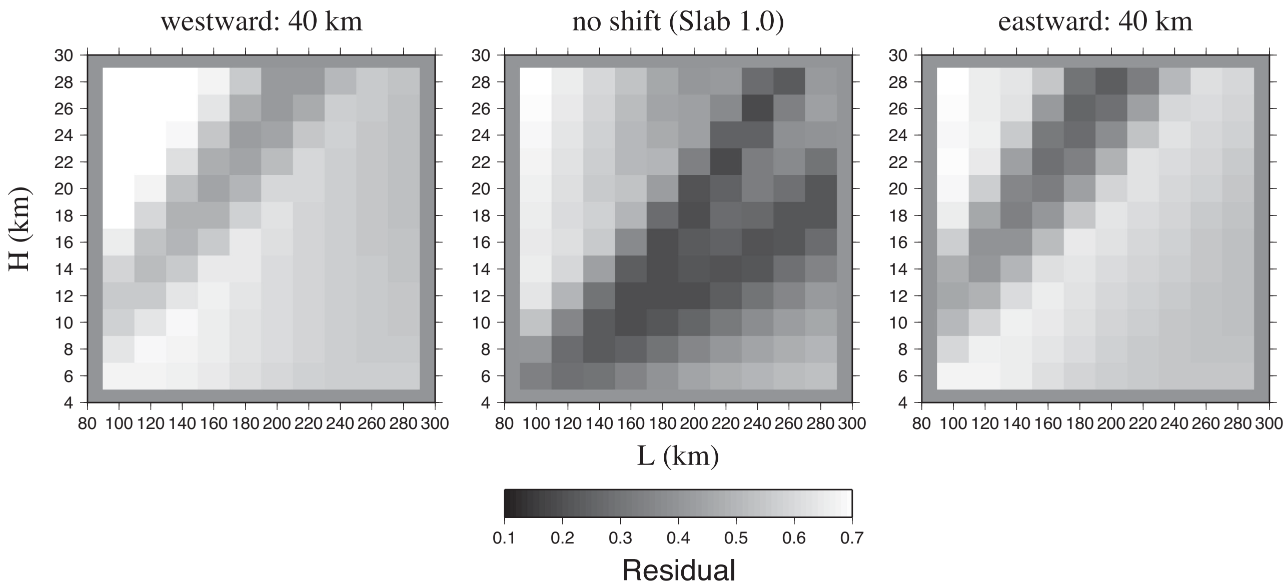

Figure 8. Residuals of all combinations of L (width) and H (height) for no shift (Slab 1.0) elevated topography case, centre and two 40 km shift cases, left and right. Darker squares represent lower residuals between synthetics and observations.

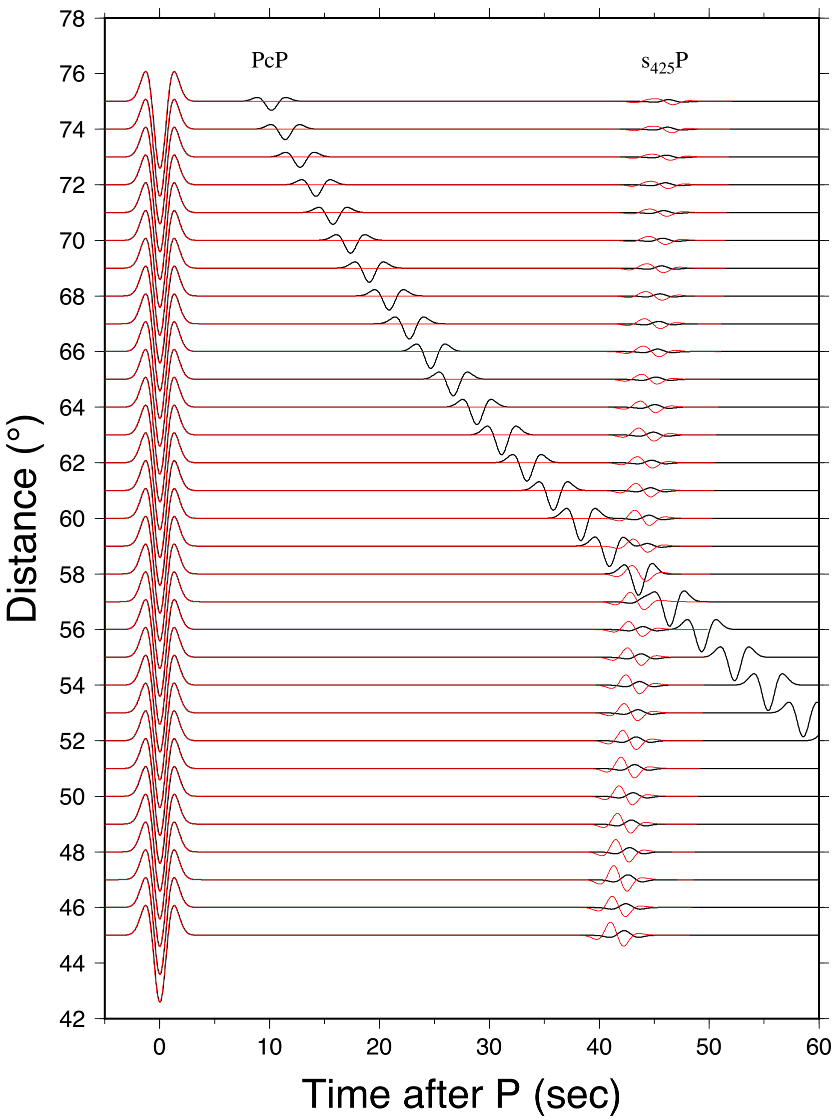

Figure 9. Record section of synthetics (red) with a ridge like elevated topography based on Slab 1.0. The height of the elevated topography is 12 km and the width is 180 km. Black lines are the result from a 1-D model with a discontinuity at a depth of 410 km.

the $s_{425}P$ ray path, if it exists, also an insufficient explanation for the large observed amplitude ratios.

The amplitude ratio also depends on the accuracy of the CMT moment tensor used to compute synthetic seismograms. If the direct *P* wave was close to the nodal plane, its amplitude should be very small, which would then result in large-amplitude ratio of $s_{425}P/P$. The CMT moment tensor we use here is displayed in Fig. 4(c) and the projected takeoff points of the direct *P* wave (black crosses) are away from the fault plane. The normal faulting focal mechanism as indicated by the CMT solution is probably reliable, as the steep downgoing *PcP* wave is clearly observed (Fig. 5a). Therefore, we take the uncertainty of CMT moment tensor as an unlikely reason for the large-amplitude ratios.

The 410 km discontinuity in this region could feature contrast stronger than 1-D reference Earth models, thus leading to larger *S*-to-*P* reflection coefficients and stronger $s_{425}P$ waves. For example, low shear velocity zones immediately above the 410 (e.g. Revenaugh & Sipkin 1994; Song *et al.* 2004) could enlarge the contrast. Song *et al.* (2004) reported an area with 5 per cent drop in shear velocity atop the 410 beneath the northwestern United States. Although their situation may be totally different from our study region, we compute the synthetics with the same amount of shear velocity drop above the 410. The result indicates that the velocity drop does enlarge the amplitude of the $s_{425}P$ wave with a factor of about 1.6 at 45°. However, our observed $s_{425}P$ wave shows amplification factors (AFs) up to 4.0. Therefore, it is less likely that an unusually large velocity contrast across the 410 plays a dominant role in the amplification.

Focusing effects from multipathing or 3-D slab wave-guiding effects may also amplify seismic waves (e.g. Weber & Wicks 1996). Weber *et al.* (2015) reported an X phase reflected from an additional piece of slab material which lags behind the direct *P* wave by about 90 s and has smaller slowness. By changing the position and dip angle of such a secondary slab fragment, it is possible to alter both traveltime and slowness of the X phase to be consistent with our measurements of high-amplitude ratios discussed above. However, the amplified converted waves remain notable across the distance range of 46°–56°. Moreover, there is no obvious deviation in the slowness or backazimuth (Fig. 5b). These two observations require a large and nearly perfect placement of a scattering

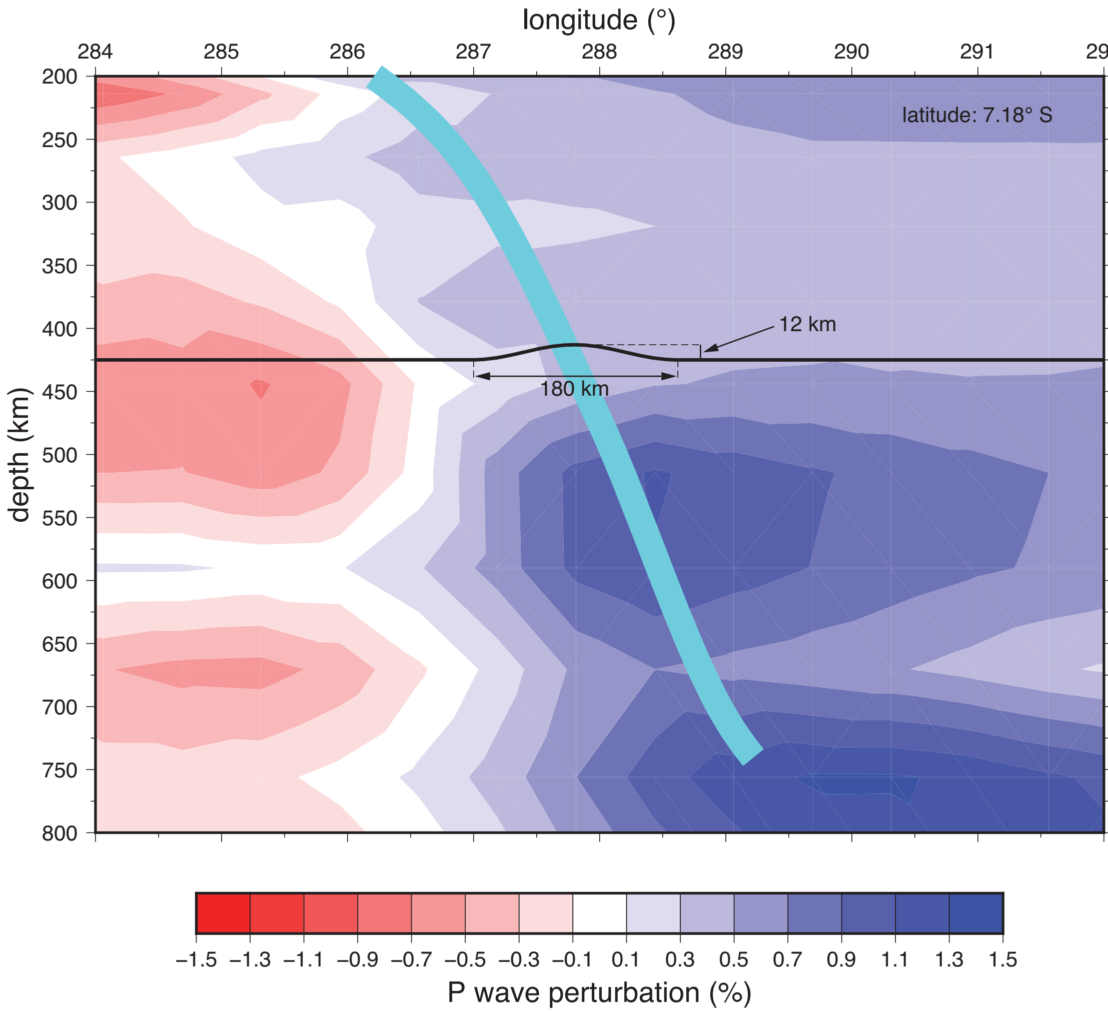

Figure 10. Topography model of a deeper 410 km discontinuity (actual depth of 425 km, solid line) overlaid over a tomography model. Tomographic model from GAP_P4 (Fukao & Obayashi 2013; Obayashi *et al.* 2013) and slab position from Slab 1.0 (Hayes *et al.* 2012) are also plotted for reference.

interface to ensure that all these recordings are focused. Since there is no additional evidence to support a second rotated slab remnant, multipathing near the source region is considered an unlikely explanation. As for 3-D effects induced by the subducted slab itself, Furumura *et al.* (2016) proposed that the subducted slab including an internal metastable olivine wedge could serve as waveguide to amplify seismic phases (Furumura & Kennett 2005). Moreover, their result indicated that surface recordings of seismic waves at 0.2–1.0 Hz could be amplified by a factor up to 1.5. The $s_{425}P$ wave in this study has a much shorter propagation distance (<200 km) inside the slab, so enhanced amplitude effects induced by the slab itself should be smaller, which then makes it an insufficient reason for the anomalous amplitude ratios we observe.

As demonstrated in Figs 3(a) and (c), the $s_{425}P$ signal could be amplified by the elevated topography of the 410. According to the phase change origin hypothesis, the 410 will be shallower at lower temperatures, therefore slab subduction may result in the elevated topography of the 410 (Helffrich 2000; Kind & Li 2007). As the *S*-to-*P* conversion points at the 410 are close to the subducted plate according to Slab 1.0 (Hayes *et al.* 2012), we propose that the focusing effect due to a locally elevated 410 km discontinuity is the reason for the large amplitude ratios.

3.3 Forward modelling

Following the reference model Slab 1.0, we adopt a ridge-like topography on the 410 (eq. 6), which strikes almost northward (Fig. 7). As Flanagan & Shearer (1998a, 1999) have demonstrated 30 km peak-to-peak global variations in the 410 topography, we explored a parameter space of ridge height H from 6 to 30 km with an interval of 2 km.The horizontal width of the ridge L is chosen in the range of 100–300 km with an interval of 20 km, because typical oceanic lithosphere thickness is about 50–100 km and diffusion should increase the thickness of the thermal anomaly. The centre frequency of Ricker wavelet is chosen as 0.3 Hz because we used a 1–5 s filter band for data processing. Synthetic seismograms of the $s_{425}P$ wave are computed in the distance range of 45°–75° with a constant azimuth of 330°, which is close to the average azimuth of the observed seismograms (Fig. 4c). The synthetics of the direct P wave are calculated with ray theory for PREM. We measure the amplitude ratios between synthetic $s_{425}P$ wave and direct P wave, and plot the ratios as a function of L and H, respectively. For given L (Fig. 6b), the amplitude ratio between the $s_{425}P$ and the direct P initially increases with increasing H, reaching a maximum at $H = 14$ km. As H increases beyond 14 km the ratio decreases until $H > 20$ for which the ratio is nearly constant. For a given H

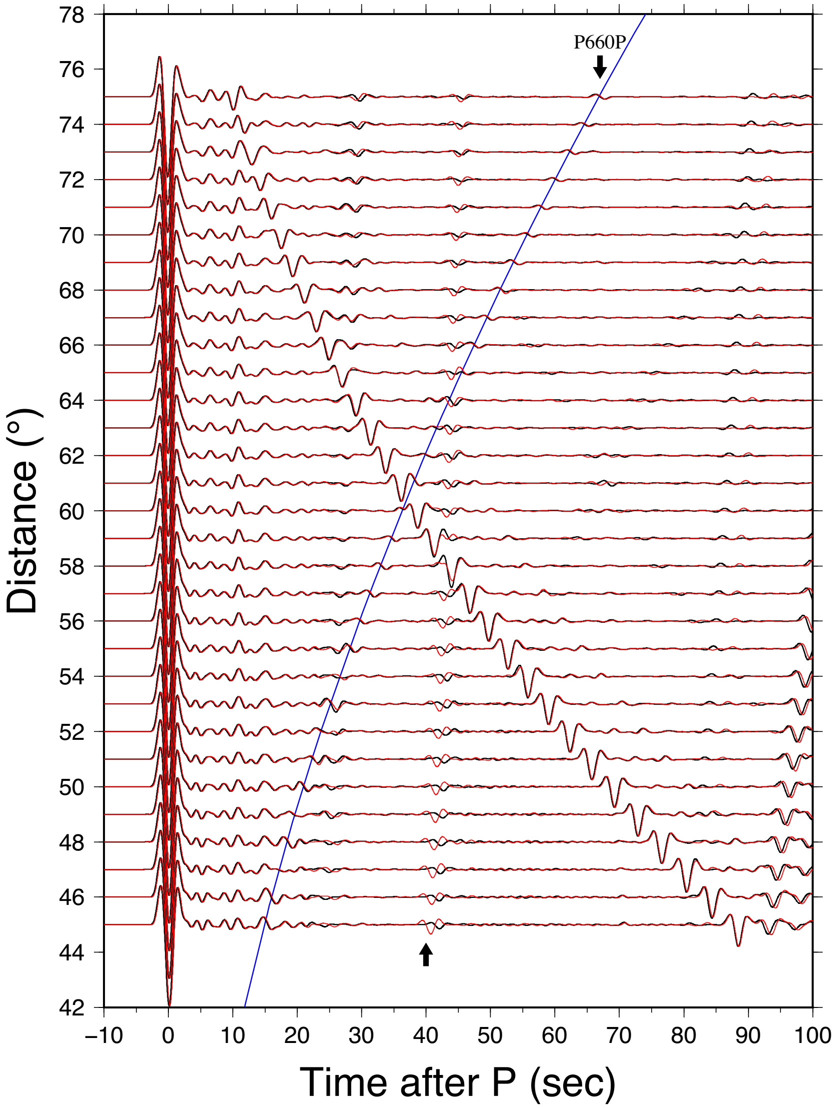

Figure 11. Record section of synthetics calculated from SEM 2-D (black for a flat 410 km discontinuity and red for a discontinuity at 425 km with elevated topography). Target phases ($s_{425}P$ or $s_{410}P$) are indicated by the black arrow. Arrival time of the $P_{660}P$ wave from IASP91 model is denoted by blue line for further explanation.

(Fig. 6c), the maximal amplitude ratio of about 0.2 occurs at about L = 180 km. These results are reasonable since larger L/H ratios lead to a 'flatter' discontinuity near the converted point of the $s_{425}P$ wave, which reduces the focusing effect. The pattern for the case of small L/H ratio is more complex. When L is small, the elevated topography will limit the area that contributes to focusing. The small ratio for large H is probably due to deconstructive interference. Therefore, a combination of H = 12–14 km and L = 160–200 km can best explain the anomalously large $s_{425}P/P$ ratio of 0.2 observed at most subarrays.

4 DISCUSSION

In order to put some constraints on the relative position of elevated topography, different ridge crest locations are tested by shifting it westward and eastward by distances of 40 and 80 km. The residuals of all combined H and L (with and without horizontal shifting) are displayed in Fig. 8. It can be seen that the no shift (Slab 1.0) case has smaller residuals than the other two shifted cases and thus we believe that the topography with 12 km height, 180 km width and horizontal location consistent with Slab1.0 provides the best match to the observations. The synthetic seismograms for this preferred model are shown in Fig. 9. The 180 km width of the elevated ridge is less than the 270–450 km wide anomaly proposed by Collier & Helffrich (1997), but it is more consistent with Flanagan & Shearer (1998b) who hypothesized that large variations in the topography of the 410 caused by a subducting slab should be limited to a narrow region (100–150 km). Furthermore, Flanagan & Shearer (1998b) also suggested a wider elevated region on the 410 for shallowly dipping slabs.

In this study, we find that the 410 km discontinuity occurs at a regional mean depth of 425 km with local elevation of 12 km (i.e. depth of 413 km, Fig. 10) near the intersection of the 410 and the subducting slab. Although the regional depth we infer is 15 km deeper than the usually assumed 410 km depth, the 425 km depth is only 7 km deeper than the corrected mean global 410 km discontinuity at 418 km (Flanagan & Shearer 1998a; Houser *et al.* 2008). The deeper discontinuity might be caused by higher temperatures of

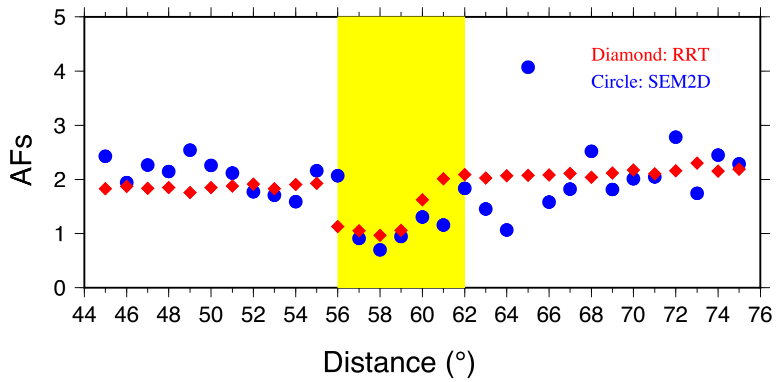

Figure 12. Amplification factors (AFs) of results for the same elevated topography calculated by Ray-based Representation Theorem (RRT) and SEM 2-D. Analogous to Fig. 6(a), yellow part marks where the $s_{425}P$ wave is contaminated by the PcP wave. Note that the $s_{425}P$ wave is also contaminated by the $P_{660}P$ wave between 63° and 65° from Fig. 11.

the Pacific mantle (Fig. 10), as suggested by relatively low seismic velocities (Fukao & Obayashi 2013; Obayashi *et al.* 2013). Collier & Helffrich (1997) reported up to 60 km elevation of the 410 near the Izu–Bonin subduction zone, substantially larger than the 12 km in this paper. This could be influenced by the different temperature of slabs in these two regions corresponding to the difference in the age of the subducting oceanic lithosphere. For example, Wiens & Gilbert (1996) found that deep earthquakes in the South American subduction zone have fewer aftershocks and proposed that it is related to warmer slab temperatures. Moreover, some studies argue that the apparent sharpness of the 410 may not be explained only by the olivine phase transitions mechanism (e.g. Petersen *et al.* 1993; Melbourne & Helmberger 1998; Lawrence & Shearer 2006; Day & Deuss 2013). For instance, water content or partial melt could play some role in modifying the contrast of the 410 km discontinuity (Helffrich & Wood 1996; Frost & Dolejs 2007; Mao *et al.* 2008).

It is possible, but unlikely, that the $s_{425}P$ signal discussed here is generated by S-to-P scattering in the lower mantle. For example, Niu (2014) attributed a scattered wave 40 s after the direct P wave to heterogeneity around a depth of 1000 km. However, we also observe a signal 20 s after the direct P wave, whose timing and slowness can be explained with the $p_{425}P$ wave (Fig. 5c). Therefore, we argue that reflection at the 410 causes the $s_{425}P$ wave. Unfortunately, the $p_{425}P$ wave is too weak for its amplitude to be reliably measured, so it does not provide a way to double check the topography variation proposed here.

In order to further validate the ray-based algorithms, we use SEM 2-D to compute synthetic seismograms for the case of an axisymmetric ridge-like topography with the same height and width of our preferred model (Komatitsch & Vilotte 1998). Fig. 11 displays the synthetic seismograms for both the ridge-like topography case (with normal discontinuity depth of 425 km, and the conversion phase is referred to as $s_{425}P$) and a 1-D model (with discontinuity depth of 410 km). The $s_{425}P$ phases are advanced and amplified compared with the $s_{410}P$ waves in the 1-D model, which is consistent with the observations. The AFs caused by the elevated structure are around 1.7–2.4 (Fig. 12), which are smaller than the results obtained using the ray-based method (Figs 6a and 9). However, after rotating the preferred 3-D topography from a strike of 30° away from great circle path to 90°, which is the case for the 2-D axisymmetric synthetics, the AFs become consistent except where the $s_{425}P$ waves are contaminated by the PcP or $P_{660}P$ waves (Figs 11 and 12).

Our algorithm is implemented only for the case of a 1-D Earth model, but it can be easily extended to the case of smoothly varying heterogeneous structures. It will fail in the case of strong anomalies such as partial melt layers (Song *et al.* 2004). Therefore, with the improvement of computational facilities, the representation theorem should be combined with FD or SEM methods, which are effective for tackling complex 3-D wave propagation, to enhance computational efficiency without compromising accuracy. Our code can be adapted for downward S-to-P conversion (e.g. $S_{660}P$) by replacing the reflection coefficient in eq. (2) with the transmission coefficient. Although our application is a near source study, our method can also be adapted for midpoint and near receiver studies (van der Lee *et al.* 1994).

5 CONCLUSIONS

We develop an algorithm for computing converted seismograms with given 3-D topography for a discontinuity above the source based on the representation theorem and ray theory. After testing dome-like and ridge-like topography, we confirm that both types of topography can amplify or weaken reflected waves substantially via focusing or defocusing effects. This suggests that amplitude information can be used to constrain undulations of mantle interfaces. As a test case, we applied this method to investigate the regional elevation of the 410 near a subducted slab beneath western Brazil. A ridge-like model with 12 km elevation across a distance of 180 km is found to match the observed amplitudes of S-to-P conversions. The inferred positive elevation is consistent with the phase change origin hypothesis of the 410, but the height of the ridge is less than the predicted value for a slab estimated to be up to 600 K cooler than ambient mantle in its core (Collier & Helffrich 2001), implying additional complexity in the formation process of the 410 topography. However, more earthquakes are needed to obtain a more spatially extensive and reliable topographic model of the 410 km discontinuity in this area.

As waveform data from more regional seismic arrays become available, weak seismic phases from conversions at mantle interfaces can be reliably retrieved. The source code of this algorithm will be posted online so the seismological community can exploit amplitude information of secondary P waves by modelling intermediate- to small-scale topography of mantle interfaces. Hopefully, the improved topography maps will help to better constrain both mantle composition and convection features.

ACKNOWLEDGEMENTS

This study is supported by China MOST 973 program (2014CB845901), the 'Strategic Priority Research Program' of the Chinese Academy of Sciences, grant no. XDB18010201, National Natural Science Foundation of China, grant nos 41322027 and NSF 1554908 (BS). All waveform data used in this study come from the Incorporated Research Institutions for Seismology (http://www.iris.edu). Some maps are generated using the Generic Mapping Tools (Wessel *et al.* 2013).

REFERENCES

Aki, K. & Richards, P.G., 2002. *Quantitative Seismology,* 2nd edn, University Science Books.

Bai, L. & Ritsema, J., 2013. The effect of large-scale shear-velocity heterogeneity on SS precursor amplitudes, *Geophys. Res. Lett.,* **40,** 6054–6058.

Benz, H.M. & Vidale, J.E., 1993. Sharpness of upper-mantle discontinuities determined from high-frequency reflections, *Nature,* **365,** 147–150.

Bina, C.R. & Wood, B.J., 1986. The 400-km seismic discontinuity and the proportion of olivine in the Earth's upper mantle, *Nature,* **324,** 449–451.

Cao, Q., van der Hilst, R.D., de Hoop, M.V. & Shim, S.-H., 2011. Seismic imaging of transition zone discontinuities suggests hot mantle west of Hawaii, *Science,* **332,** 1068–1071.

Cerveny, V., 2005. *Seismic Ray Theory Book,* Cambridge Univ. Press.

Chaljub, E. & Tarantola, A., 1997. Sensitivity of SS precursors to topography on the upper-mantle 660-km discontinuity, *Geophys. Res. Lett.,* **24,** 2613–2616.

Chambers, K., Woodhouse, J.H. & Deuss, A., 2005. Topography of the 410-km discontinuity from PP and SS precursors, *Earth planet. Sci. Lett.,* **235,** 610–622.

Chapman, C.H., 1978. A new method for computing synthetic seismograms, *Geophys. J. Int.,* **54,** 481–518.

Chapman, C.H. & Drummond, R., 1982. Body-wave seismograms in inhomogeneous media using Maslov asymptotic theory, *Bull. seism. Soc. Am.,* **72,** S277–S317.

Chu, R., Schmandt, B. & Helmberger, D.V., 2012. Upper mantle P velocity structure beneath the Midwestern United States derived from triplicated waveforms, *Geochem. Geophys. Geosyst.,* **13,** 1–21.

Collier, J.D. & Helffrich, G.R., 1997. Topography of the 410 and 660 km seismic discontinuities in the Izu-Bonin subduction zone, *Geophys. Res. Lett.,* **24,** 1535–1538.

Collier, J.D. & Helffrich, G.R., 2001. The thermal influence of the subducting slab beneath South America from 410 and 660 km discontinuity observations, *Geophys. J. Int.,* **147,** 319–329.

Davis, J.P., Kind, R. & Sacks, I.S., 1989. Precursors to P′P′ re-examined using broad-band data, *Geophys. J. Int.,* **99,** 595–604.

Day, E.A. & Deuss, A., 2013. Reconciling PP and P′P′ precursor observations of a complex 660 km seismic discontinuity, *Geophys. J. Int.,* **194,** 834–838.

Deng, K. & Zhou, Y., 2015. Wave diffraction and resolution of mantle transition zone discontinuities in receiver function imaging, *Geophys. J. Int.,* **201,** 2008–2025.

Deuss, A., Redfern, S.A.T., Chambers, K. & Woodhouse, J.H., 2006. The nature of the 660-kilometer discontinuity in Earth's mantle from Global Seismic Observations of PP precursors, *Science,* **311,** 198–201.

Dziewonski, A.M. & Anderson, D.L., 1981. Preliminary reference Earth model, *Phys. Earth planet. Inter.,* **25,** 297–356.

Dziewonski, A.M., Chou, T.-A. & Woodhouse, J.H., 1981. Determination of earthquake source parameters from waveform data for studies of global and regional seismicity, *J. geophys. Res.,* **86,** 2825–2852.

Earle, P.S. & Shearer, P.M., 1997. Observations of PKKP precursors used to estimate small-scale topography on the core-mantle boundary, *Science,* **277,** 667–670.

Ekström, G., Nettles, M. & Dziewoński, A.M., 2012. The global CMT project 2004–2010: centroid-moment tensors for 13,017 earthquakes, *Phys. Earth planet. Inter.,* **200,** 1–9.

Flanagan, M.P. & Shearer, P.M., 1998a. Global mapping of topography on transition zone velocity discontinuities by stacking SS precursors, *J. geophys. Res.,* **103,** 2673–2692.

Flanagan, M.P. & Shearer, P.M., 1998b. Topography on the 410-km seismic velocity discontinuity near subduction zones from stacking of sS, sP, and pP precursors, *J. geophys. Res.,* **103,** 21 165–21 182.

Flanagan, M.P. & Shearer, P.M., 1999. A map of topography on the 410-km discontinuity from PP precursors, *Geophys. Res. Lett.,* **26,** 549–552.

Frost, D.J. & Dolejs, D., 2007. Experimental determination of the effect of H_2O on the 410-km seismic discontinuity, *Earth planet. Sci. Lett.,* **256,** 182–195.

Fukao, Y. & Obayashi, M., 2013. Subducted slabs stagnant above, penetrating through, and trapped below the 660 km discontinuity, *J. geophys. Res.,* **118,** 5920–5938.

Furumura, T. & Kennett, B.L.N., 2005. Subduction zone guided waves and the heterogeneity structure of the subducted plate: intensity anomalies in northern Japan, *J. geophys. Res.,* **110,** 1–27.

Furumura, T., Kennett, B.L.N. & Padhy, S., 2016. Enhanced waveguide effect for deep-focus earthquakes in the subducting Pacific slab produced by a metastable olivine wedge, *J. geophys. Res.,* **121,** 6779–6796.

Haskell, N.A., 1964. Radiation pattern of surface waves from point sources in a multi-layered medium, *Bull. seism. Soc. Am.,* **54,** 377–393.

Hayes, G.P., Wald, D.J. & Johnson, R.L., 2012. Slab1.0: a three-dimensional model of global subduction zone geometries, *J. geophys. Res.,* **117,** B01302, doi:10.1029/2011JB008524.

Helffrich, G.R., 2000. Topography of the transition zone seismic discontinuities, *Rev. Geophys.,* **38,** 141–158.

Helffrich, G.R. & Bina, C.R., 1994. Frequency dependence of the visibility and depths of mantle seismic discontinuities, *Geophys. Res. Lett.,* **21,** 2613–2616.

Helffrich, G.R. & Wood, B.J., 1996. 410 km discontnuity sharpness and the form of the olivine alpha-beta phase diagram: resolution of apparent seismic contradictions, *Geophys. J. Int.,* **126**(2), F7–F12.

Helffrich, G.R., Asencio, E., Knapp, J. & Owens, T., 2003. Transition zone structure in a tectonically inactive area: 410 and 660 km discontinuity properties under the northern North Sea, *Geophys. J. Int.,* **155,** 193–199.

Houser, C., Masters, G., Flanagan, M. & Shearer, P., 2008. Determination and analysis of long-wavelength transition zone structure using SS precursors, *Geophys. J. Int.,* **174,** 178–194.

Igel, H. & Weber, M., 1995. SH wave propagation in the whole mantle using high order finite differences, *Geophys. Res. Lett.,* **22,** 731–734.

Irifune, T., Nishiyama, N., Kuroda, K., Inoue, T., Isshiki, M., Utsumi, W. & Ohtaka, O., 1998. The postspinel phase boundary in Mg_2SiO_4 determined by in situ X-ray diffraction, *Science,* **279,** 1698–1700.

Ishii, M. & Tromp, J., 1999. Normal-mode and free-air gravity constraints on lateral variations in velocity and density of Earth's Mantle, *Science,* **285,** 1231–1236.

Kampfmann, W. & Muller, G., 1989. PcP amplitude calculations for a core-mantle boundary with topography, *Geophys. Res. Lett.,* **16,** 653–656.

Kennett, B.L.N., Engdahl, E.R. & Buland, R., 1995. Constraints on seismic velocities in the Earth from traveltimes, *Geophys. J. Int.,* **122,** 108–124.

Kikuchi, M. & Kanamori, H., 1982. Inversion of complex body waves, *Bull. seism. Soc. Am.,* **72,** 491–506.

Kind, R. & Li, X., 2007. Deep Earth structure—transition zone and mantle discontinuities, in *Treatise on Geophysics,* Vol. 1, pp. 591–618, eds Romanowicz, B. & Dziewonski, A., Elsevier.

Komatitsch, D. & Vilotte, J.P., 1998. The spectral element method: an efficient tool to simulate the seismic response of 2D and 3D geological structures, *Bull. seism. Soc. Am.,* **88,** 368–392.

Komatitsch, D. & Tromp, J., 1999. Introduction to the spectral element method for three-dimensional seismic wave propagation, *Geophys. J. Int.,* **139,** 809–822.

Lawrence, J.F. & Shearer, P.M., 2006. Constraining seismic velocity and density for the mantle transition zone with reflected and transmitted waveforms, *Geochem. Geophys. Geosyst.,* **7**(10), doi:10.1029/2006GC001339.

Lay, T., Williams, Q. & Garnero, E.J., 1998. The core–mantle boundary layer and deep Earth dynamics, *Nature,* **392,** 461–468.

Lessing, S., Thomas, C., Saki, M., Schmerr, N. & Vanacore, E., 2015. On the difficulties of detecting PP precursors, *Geophys. J. Int.,* **201,** 1666–1681.

Li, X., Sobolev, S.V., Kind, R., Yuan, X. & Estabrook, C., 2000. A detailed receiver function image of the upper mantle discontinuities in the Japan subduction zone, *Earth planet. Sci. Lett.,* **183,** 527–541.

Li, J., Chen, Q., Vanacore, E. & Niu, F., 2008. Topography of the 660-km discontinuity beneath northeast China: implications for a retrograde motion of the subducting Pacific slab, *Geophys. Res. Lett.,* **35,** L01302, doi:10.1029/2007GL031658.

Mao, Z., Jacobsen, S.D., Jiang, F., Smyth, J.R., Holl, C.M. & Duffy, T.S., 2008. Elasticity of hydrous wadsleyite to 12 GPa: implications for Earth's transition zone, *Geophys. Res. Lett.,* **35,** L21305, doi:10.1029/2008GL035618.

Melbourne, T. & Helmberger, D., 1998. Fine structure of the 410-km discontinuity, *J. geophys. Res.,* **103,** 10 091–10 102.

Neuberg, J. & Lisapaly, L., 1997. Kirchhoff synthetics for seismic reflections and diving waves in two dimensions and application to the D'layer, *Geophys. J. Int.,* **129,** 587–596.

Ni, S., Ding, X., Helmberger, D.V. & Gurnis, M., 1999. Low-velocity structure beneath Africa from forward modeling, *Earth planet. Sci. Lett.,* **170,** 497–507.

Ni, S., Tan, E., Gurnis, M. & Helmberger, D., 2002. Sharp sides to the African superplume, *Science,* **296,** 1850–1852.

Niu, F., 2014. Distinct compositional thin layers at mid-mantle depths beneath northeast China revealed by the USArray, *Earth planet. Sci. Lett.,* **402,** 305–312.

Obayashi, M., Yoshimitsu, J., Nolet, G., Fukao, Y., Shiobara, H., Sugioka, H., Miyamachi, H. & Gao, Y., 2013. Finite frequency whole mantle P wave tomography: improvement of subducted slab images, *Geophys. Res. Lett.,* **40,** 5652–5657.

Petersen, N., Vinnik, L., Kosarev, G., Kind, R., Oreshin, S. & Stammler, K., 1993. Sharpness of the mantle discontinuities, *Geophys. Res. Lett.,* **20,** 859–862.

Revenaugh, J. & Sipkin, S.A., 1994. Seismic evidence for silicate melt atop the 410-km mantle discontinuity, *Nature,* **369,** 474–476.

Ringwood, A.E., 1969. Phase transformations in the mantle, *Earth planet. Sci. Lett.,* **5,** 401–412.

Ritsema, J., van Heijst, H.J. & Woodhouse, J.H., 1999. Complex shear wave velocity structure imaged beneath Africa and Iceland, *Science,* **286,** 1925–1928.

Rost, S. & Thomas, C., 2002. Array seismology: methods and applications, *Rev. Geophys.,* **40,** 1008, doi:10.1029/2000RG000100.

Rost, S. & Revenaugh, J., 2004. Small-scale changes of core-mantle boundary reflectivity studied using core reflected PcP, *Phys. Earth planet. Inter.,* **145,** 19–36.

Schmandt, B., Jacobsen, S.D., Becker, T.W., Liu, Z. & Dueker, K.G., 2014. Dehydration melting at the top of the lower mantle, *Science,* **344,** 1265–1268.

Schmerr, N. & Garnero, E.J., 2007. Upper mantle discontinuity topography from thermal and chemical heterogeneity, *Science,* **318,** 623–626.

Schmerr, N.C., Kelly, B.M. & Thorne, M.S., 2013. Broadband array observations of the 300 km seismic discontinuity, *Geophys. Res. Lett.,* **40,** 841–846.

Shen, Z., Ni, S., Wu, W. & Sun, D., 2016. Short period ScP phase amplitude calculations for core-mantle boundary with intermediate scale topography, *Phys. Earth planet. Inter.,* **253,** 64–73.

Song, T.-R.A., Helmberger, D.V. & Grand, S.P., 2004. Low-velocity zone atop the 410-km seismic discontinuity in the northwestern United States, *Nature,* **427,** 530–533.

Thompson, D.A., Helffrich, G., Bastow, I.D., Kendall, J.-M., Wookey, J., Eaton, D.W. & Snyder, D.B., 2011. Implications of a simple mantle transition zone beneath cratonic North America, *Earth planet. Sci. Lett.,* **312,** 28–36.

Tibi, R. & Wiens, D.A., 2005. Detailed structure and sharpness of upper mantle discontinuities in the Tonga subduction zone from regional broadband arrays, *J. geophys. Res.,* **110,** B06313, doi:10.1029/2004JB003433.

Tsuboi, S., Komatitsch, D., Ji, C. & Tromp, J., 2004. Modeling of global seismic wave propagation on the Earth Simulator, *J. Earth Simul.,* **1,** 57–66.

van der Lee, S., Paulssen, H. & Nolet, G., 1994. Variability of P660s phases as a consequence of topography of the 660 km discontinuity, *Phys. Chem. Deep Earth,* **86,** 147–164.

Wang, B. & Niu, F., 2010. A broad 660 km discontinuity beneath northeast China revealed by dense regional seismic networks in China, *J. geophys. Res.,* **115,** B06308, doi:10.1029/2009JB006608.

Wang, Y., Grand, S.P. & Tang, Y., 2014. Shear velocity structure and mineralogy of the transition zone beneath the East Pacific Rise, *Earth planet. Sci. Lett.,* **402,** 313–323.

Weber, M., Wicks, C., Jr., Le Stunff, Y., Romanowicz, B. & Kruger, F., 2015. Seismic evidence for a steeply dipping reflector–stagnant slab in the mantle transition zone, *Geophys. J. Int.,* **200,** 1235–1251.

Weber, M. & Wicks, C.W., Jr., 1996. Reflections from a distant subduction zone, *Geophys. Res. Lett.,* **23**(12), 1453–1456.

Weidner, D.J. & Wang, Y., 1998. Chemical- and Clapeyron-induced buoyancy at the 660 km discontinuity, *J. geophys. Res.,* **103,** 7431–7441.

Weidner, D.J. & Wang, Y., 2000. Phase transformations: implications for mantle structure, in *Earth's Deep Interior: Mineral Physics and Tomography From the Atomic to the Global Scale*, pp. 215–235, eds Karato, S.-I., Forte, A., Liebermann, R., Masters, G. & Stixrude, L., American Geophysical Union, Washington.

Wessel, P., Smith, W.H.F., Scharroo, R., Luis, J. & Wobbe, F., 2013. Generic mapping tools: improved version released, *EOS, Trans. Am. geophys. Un.,* **94,** 409–410.

Wicks, C.W., Jr. & Richards, M.A., 1993. A detailed map of the 660-kilometer discontinuity beneath the Izu-Bonin subduction zone, *Science,* **261,** 1424–1427.

Wiens, D.A. & Gilbert, H.J., 1996. Effect of slab temperature on deep-earthquake aftershock productivity and magnitude-frequency relations, *Nature,* **384,** 153–156.

Wu, W., Ni, S. & Shen, Z., 2014. Constraining the short scale core–mantle boundary topography beneath Kenai Peninsula (Alaska) with amplitudes of core-reflected PcP wave, *Phys. Earth planet. Inter.,* **236,** 60–68.

Xu, F., Vidale, J.E. & Earle, P.S., 2003. Survey of precursors to P′P′: fine structure of mantle discontinuities, *J. geophys. Res.,* **108,** 2024, doi:10.1029/2001JB000817.

Zhu, L. & Rivera, L.A., 2002. A note on the dynamic and static displacements from a point source in multilayered media, *Geophys. J. Int.,* **148,** 619–627.